

Imaging flat band electron hydrodynamics in biased bilayer graphene

Canxun Zhang,^{1,*} Evgeny Redekop,^{1,*} Hari Stoyanov,^{1,*} Jack H. Farrell,² Sunghoon Kim,¹ Ludwig Holleis,¹ David Gong,¹ Aidan Keough,¹ Youngjoon Choi,¹ Takashi Taniguchi,³ Kenji Watanabe,⁴ Martin E. Huber,⁵ Ania C. Bleszynski Jayich,¹ Andrew Lucas,² and Andrea F. Young^{1,†}

¹*Department of Physics, University of California, Santa Barbara, California 93106, USA*

²*Department of Physics and Center for Theory of Quantum Matter, University of Colorado, Boulder, Colorado 80309, USA*

³*Research Center for Materials Nanoarchitectonics, National Institute for Materials Science, 1-1 Namiki, Tsukuba 305-0044, Japan*

⁴*Research Center for Electronic and Optical Materials, National Institute for Materials Science, 1-1 Namiki, Tsukuba 305-0044, Japan*

⁵*Departments of Physics and Electrical Engineering, University of Colorado, Denver, Colorado 80204, USA*

Hydrodynamic electron transport arises when carrier kinetics are dominated by interelectron collisions rather than the relaxation of momentum out of the electron system[1]. In recent years, signatures of electron hydrodynamics have been reported in graphene devices[2–14] owing to the low disorder and weak electron–phonon coupling. However, these experiments have been performed in regimes where the carrier mass is light, and the electron–electron collision length—though smaller than corresponding lengths for phonon or impurity scattering—remains large in absolute terms, typically several hundred nanometers. This restricts hydrodynamic transport phenomena to large length scales, limiting miniaturization of devices based on hydrodynamic flow. The advent of dual-gated rhombohedral graphene multilayers introduces a new route toward enhanced hydrodynamic behavior via their large—and tunable—effective mass[15]. Here, we employ a scanning superconducting magnetic sensor[16, 17] to image local current flow in dual-gated bilayer graphene. Exploiting a sample geometry sensitive to both laminar and vortical flow[13, 18], we identify three distinct transport regimes—ballistic, hydrodynamic, and diffusive—across the full phase space spanned by carrier density and displacement field. The strongest hydrodynamic transport is observed in the flat band regime, where fitting our results to a unified Boltzmann transport model reveals the electron–electron scattering length to be comparable to the Fermi wavelength of ~ 50 nm. High-current measurements, meanwhile, reveal striking nonlinearities in the flow pattern. Our results pave the way for miniaturized electronic devices based on linear and nonlinear electron hydrodynamics.

Hydrodynamics is a universal framework that describes how conserved quantities such as momentum evolve toward local equilibrium in thermalizing many-body systems[19, 20]. Electrons in solids typically equilibrate with each other via momentum-conserving electron–electron scattering, parameterized by a length scale, ℓ_{ee} [1]. For hydrodynamic flow of electrons to be observed, ℓ_{ee} must be the shortest scattering length at play; in particular it must be smaller than both the device size L and ℓ_{mr} , the length scale associated with relaxation of momentum to an external bath. In ordinary metals, $\ell_{mr} \ll \ell_{ee}, L$ due to scattering from phonons and disorder as well as Umklapp processes, leading to diffusive transport. In graphene[21, 22], the absence of two-body Umklapp scattering, weak electron–phonon coupling, and continuous improvements in material quality now allow for ℓ_{mr} to far exceed the typical device size of $L \approx 10 \mu\text{m}$ over a wide range of temperatures. Past experiments have shown that, while at low temperatures transport is ballistic (i.e., $\ell_{mr}, \ell_{ee} \gg L$), increasing the temperature can lower ℓ_{ee} sufficiently to enable the observation of hydrodynamic effects[2–14]. Quantitatively, however, these experiments found $\ell_{ee} \gtrsim 250$ nm, limited by the eventual onset of phonon scattering. This precludes further device

miniaturization and restricts the range over which emergent hydrodynamic parameters, such as viscosity, can be tuned in experiments.

In a two-dimensional Fermi liquid with parabolic dispersion,

$$\ell_{ee} \propto \frac{|n_e|^{3/2}}{m^* T^2}, \quad (1)$$

where n_e is the carrier density, m^* is the effective mass, and T is the temperature[1, 23]. The large ℓ_{ee} characterizing past experiments in graphene can be tied to the fact that m^* is small. In rhombohedral (ABC-stacked) multilayer graphene, including AB-stacked bilayer (R2G; Fig. 1a), the electronic structure features two low-energy bands with an effective mass that can be tuned by over one order of magnitude as a function of n_e and displacement field D [15], both of which can be controlled by the electric field effect in dual-gated devices. At $D = 0$ (the regime of past experiments[2, 5]), the band structure is semimetallic, with $m^* \approx 0.05m_e$ where m_e is the free electron mass (Fig. 1b,c). Ballistic transport is thus expected at low temperatures, except near the charge neutrality point (CNP), where transport is instead dominated by electron–hole recombination. At large D , in contrast, the interlayer potential difference Δ_U produces both a

band gap and band edge van Hove singularities which increase m^* to values comparable to or even larger than m_e . Per Eq. (1), these flat band regions should be highly favorable to hydrodynamic transport.

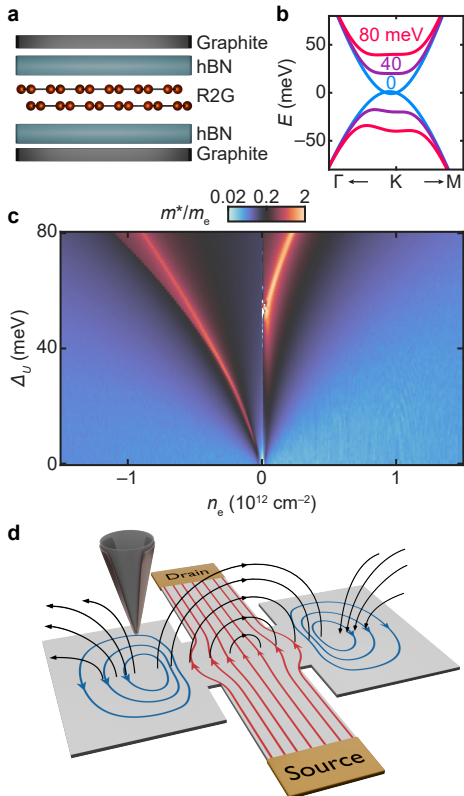


FIG. 1. **Tunable effective mass in dual-gated R2G.** **a**, Schematic view of a dual-gated R2G device. Two graphite gates, separated from the R2G flake by hexagonal boron nitride (hBN) dielectrics, together control the carrier density n_e and the applied displacement field D . **b**, Single-particle band structure of R2G near the Brillouin zone corner calculated within a tight-binding model[24]. Different curves correspond to different values of interlayer potential difference $\Delta_U \propto D$. **c**, Density of states effective mass m^* as a function of n_e and Δ_U . **d**, Illustration of the experimental geometry, showing nSOT sensor, current streamlines (red and blue), and flux lines associated with the fringe magnetic field (black).

Complicating this naive picture, however, is the onset of Fermi surface reconstructions due to Stoner ferromagnetism at large m^* . Experiments in dual-gated R2G have revealed a complex low-temperature phase diagram of correlated ferromagnetic phases with broken spin and/or valley symmetries[25–31]. Notably, the resistance in the metallic high-temperature parent phase of these magnets was observed to show a negative temperature coefficient, $dR/dT < 0$ [32, 33]. This behavior is reminiscent of the hydrodynamic Gurzhi effect[1] where the declining viscosity of the electron fluid leads to a negative temperature coefficient[34, 35]. However, negative temperature coefficients have also been observed near the Curie tem-

perature in elemental rare-earth magnets[36], where this behavior is attributed to reduced ℓ_{mr} due to scattering of electrons by magnetic fluctuations that subsequently relax their momentum via Umklapp processes[37]. While these mechanisms produce similar behavior of the global resistivity, they are expected to generate qualitatively distinct microscopic current profiles.

Here, we use a superconducting sensor[16, 17] to measure the fringe magnetic field above a dual-gated R2G device, which we then use to reconstruct the in-plane current profile on the nanoscale as a function of n_e and D (Methods). A key challenge in spatially resolved measurements of this kind is to successfully disambiguate all three (hydrodynamic, ballistic, and diffusive) transport regimes. Our sample geometry is shown in Fig. 1d, and features both a fixed-width channel ($w \approx 1.15 \mu\text{m}$) and two lateral chambers connected to the channel by constrictions of $d \approx 1.0 \mu\text{m}$ (Methods, Extended Data Fig. 1). Electron transport in the channel distinguishes hydrodynamic flow, characterized by a Poiseuille velocity profile with a higher current density in the center, from ballistic or diffusive behavior with flatter or even concave profiles[1, 6, 7, 11, 38]. In contrast, current flow in the lateral chambers probes the local violation of Ohm’s law—stationary vortices or whirlpools can emerge in either the ballistic or hydrodynamic regime[2, 4, 13, 18, 22, 38] but are forbidden when transport is diffusive on short length scales. Cross-correlating flow patterns in the channel and chambers can thus be used to unambiguously determine the nature of the carrier kinetics.

IMAGING LOCAL CURRENT FLOW

Figure 2a shows a spatial map of the current density along the channel direction, $J_y(x, y)$, for a total applied current of $I_0 \approx 4.5 \mu\text{A}$ at the CNP and the value of D corresponding to $\Delta_U = 0$. $J_y(x, y)$ is determined from the measured B field (shown in Extended Data Fig. 2 along with the corresponding $J_x(x, y)$) by standard Fourier domain techniques (Methods). A complementary visualization is provided by the streamline plot shown in Fig. 2b, in which each red line represents $I_0/20$. At the CNP, streamlines in the center of the channel follow a straight path, but those at the left and right extremes take a slight detour into the chambers. Qualitatively, the flow pattern is fully laminar, in accordance with local Ohm’s law $\mathbf{J} = -\sigma \nabla \phi$ where σ is the local conductivity and ϕ is the local electric potential. A different picture emerges under heavy electron or hole doping, shown in Fig. 2c,d for $n_e = -1.3 \times 10^{12} \text{cm}^{-2}$ and $D = 0.39 \text{V/nm}$. Here, J_y in the channel resembles that at the CNP, but the streamline plot reveals closed loops of current within the chambers (here each blue line represents $I_0/200$). A third qualitatively distinct regime is found at high D and low $|n_e|$, corresponding to the flat band regime. Figure 2e,f

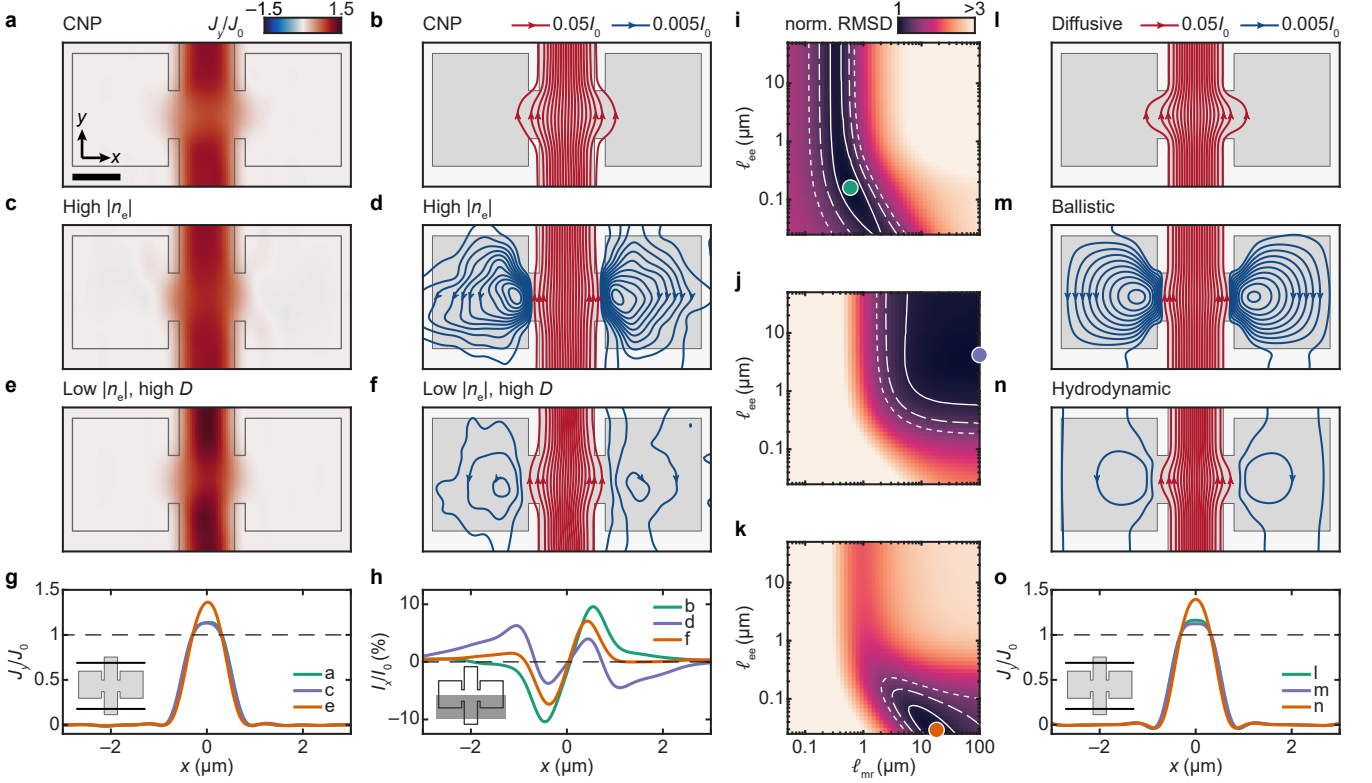


FIG. 2. **Contrasting microscopic transport regimes.** **a**, Reconstructed current density $J_y(x, y)$ at $n_e = 0 \times 10^{12} \text{ cm}^{-2}$ and $D = 0 \text{ V/nm}$, where R2G is a charge-neutral gapless semimetal. Scale bar: $1 \mu\text{m}$. J_y is normalized by $J_0 \equiv I_0/w$, the average current density in the channel. **b**, Current streamlines at the same n_e and D as panel **a**. **c**, $J_y(x, y)$ for $n_e = -1.3 \times 10^{12} \text{ cm}^{-2}$ and $D = 0.39 \text{ V/nm}$. **d**, Current streamlines at the same n_e and D as panel **c**. **e**, $J_y(x, y)$ for $n_e = -0.4 \times 10^{12} \text{ cm}^{-2}$ and $D = 0.39 \text{ V/nm}$. **f**, Current streamlines at the same n_e and D as panel **e**. **g**, $J_y(x)/J_0$ averaged between measurements at $y = \pm 2 \mu\text{m}$ (see inset) for the data in panels **a**, **c**, and **e** as marked. **h**, Normalized transverse current $I_x(x)/I_0$ (see inset and Eq. (2) of main text) corresponding to the data in panels **b**, **d**, and **f** as marked. **i**, Combined root mean square deviation (RMSD) between experimental data at $n_e = 0 \times 10^{12} \text{ cm}^{-2}$ and $D = 0 \text{ V/nm}$ and the Boltzmann model parameterized by ℓ_{mr} and ℓ_{ee} . The RMSD is normalized by the minimum value, indicated by the dot and corresponding to the best fit. Contours of 1.1, 1.3, and 1.5 delineate phenomenological confidence intervals. **j**, RMSD for $n_e = -1.3 \times 10^{12} \text{ cm}^{-2}$ and $D = 0.39 \text{ V/nm}$. **k**, RMSD for $n_e = -0.4 \times 10^{12} \text{ cm}^{-2}$ and $D = 0.39 \text{ V/nm}$. **l**, Theoretical current streamlines for $\ell_{\text{mr}} = 600 \text{ nm}$ and $\ell_{\text{ee}} = 161 \text{ nm}$, corresponding to the best fit in panel **i**. **m**, Theoretical current streamlines for $\ell_{\text{mr}} = 100 \mu\text{m}$ and $\ell_{\text{ee}} = 4.2 \mu\text{m}$, corresponding to the best fit in panel **j**. **n**, Theoretical current streamlines for $\ell_{\text{mr}} = 18.2 \mu\text{m}$ and $\ell_{\text{ee}} = 29 \text{ nm}$, corresponding to the best fit in panel **k**. **o**, $J_y(x)/J_0$ at $y = \pm 2 \mu\text{m}$ for the best fits described in panels **l**, **m** and **n**.

show J_y and the streamlines for $n_e = -0.4 \times 10^{12} \text{ cm}^{-2}$ and $D = 0.39 \text{ V/nm}$. Within the channel, J_y is significantly concentrated away from the boundaries, while vortical flow is still present in the chambers, albeit with quantitatively distinct strength and spatial distribution.

We define two empirical metrics that capture both the laminar channel flow and vortical chamber flow. The channel flow profile is characterized by $J_y(x)$ measured far from the entrance to lateral chambers (near $y = \pm 2 \mu\text{m}$). As shown in Fig. 2g, the flat band regime features a current profile with approximately 30% higher concentration than the average current density J_0 (dashed line). This contrasts with the much flatter distribution observed for both the CNP and high-density regimes. To quantify the vortex profile, we plot the

“transverse current” I_x (Fig. 2h), defined as

$$I_x(x) := \frac{\int_{-y_0}^0 J_x(x, y) dy - \int_0^{y_0} J_x(x, y) dy}{2}, \quad (2)$$

where $y_0 = 2 \mu\text{m}$. Physically, I_x counts the total current (i.e., number of streamlines) passing through a vertical cross-section at position x . At the CNP, where no vorticity is expected or observed in the streamlines, I_x is positive for positive x and negative for negative x . Vortical flow, in contrast, introduces sign changes in I_x . The magnitude of this sign-changing signal provides an approximate metric for the vortex strength while the position of the extrema is closely correlated with the vortex center. Evidently, between the high- $|n_e|$ regime of Fig. 2c,d and the flat band regime of Fig. 2e,f, the vortical flow de-

creases in strength while the vortex center moves further into the chambers.

To quantify these behaviors, we compare experimental data with a phenomenological Boltzmann transport model applied to the experimental sample geometry, in which scattering is parameterized by free parameters ℓ_{mr} and ℓ_{ee} under a two-rate relaxation time approximation (Methods). We take the boundary scattering to be fully diffusive, based both on previous literature on etched graphene edges[6] and on a comparison of the fits deep in the ballistic regime of high $|n_e|$ (see Extended Data Fig. 3). We fit our data by calculating root mean square deviations (RMSDs) between experiment and theory for the J_y/J_0 and I_x/I_0 (one-dimensional) curves, and combining these RMSDs into a single figure of merit which we then normalize by the minimum value for a given data set (Methods). This combined RMSD is plotted as a function of ℓ_{mr} and ℓ_{ee} in Fig. 2i–k for the data of panels g and h. These figures also show contours defining “confidence intervals” corresponding to where the RMSD exceeds the minimum by 10%, 30%, and 50%.

At the CNP (Fig. 2i), the best fit is achieved for ℓ_{mr} on the order of a few hundred nanometers while ℓ_{ee} is comparatively unconstrained. This is consistent with a diffusive regime dominated by momentum-relaxing scattering, as expected at the CNP where coexisting electrons and holes relax the current even at low temperatures. At high $|n_e|$ (Fig. 2j), the best fit is obtained for simultaneously large ℓ_{mr} and ℓ_{ee} , i.e., this regime is ballistic and the strong vortical flow arises from ballistic carrier trajectories scattering off the chamber boundaries. Finally, in the high- D , low- $|n_e|$ regime (Fig. 2k), the Boltzmann fit finds a large $\ell_{\text{mr}} \gtrsim L$ while ℓ_{ee} is as small as 50 nm. This large separation in scattering lengths implies that the flow is deep in the hydrodynamic regime, where momentum-conserving collisions dominate transport and the current pattern is determined by the Gurzhi length, $\sqrt{\ell_{\text{ee}}\ell_{\text{mr}}}/2 \approx 360$ nm. The assignment of these three flow regimes is further supported by direct visualization of the calculated current distributions at the best-fit parameters (dots in Fig. 2i–k). The streamline plots of Fig. 2l–n exhibit strong/weak vortical flow in the ballistic/hydrodynamic regime and an absence of vortical flow in the diffusive regime, in qualitative agreement with the experimental maps of Fig. 2b,d,f. Calculated $J_y(x)/J_0$ (Fig. 2o) similarly agrees with the Poiseuille flow in the channel for the hydrodynamics regime. (See Extended Data Figs. 4, 5 for additional details of the fitting.)

FLOW REGIME PHASE DIAGRAM

The quantitative analysis developed for the three (n_e, D) points described in Fig. 2 can be extended across the full parameter space to map the domains of ballistic, hydrodynamic, and diffusive transport. At a qualitative

level, the evolution of flow patterns can be characterized by two further simplified quantities. Flow concentration is defined by $J_y(x=0)/J_0$, i.e., the enhancement of current flow at the channel center. The “counterflow %”, meanwhile, is defined by I_x evaluated at $|x| = 1.3 \mu\text{m}$ and antisymmetrized between the two chambers; this approximates the total loop current near the vortex center. Figure 3a,b show the flow concentration and counterflow % as a function of n_e and D . Evidently, the three representative points of Fig. 2 lie within broad domains of stability, with high $|n_e|$ characterized by strong counterflow and low flow concentration, lower $|n_e|$ and high D characterized by weak counterflow and high concentration, and a small regime at the CNP and low D showing neither positive counterflow nor high concentration.

Fitting data taken across the entire phase space to the Boltzmann model allows us to directly constrain the transport length scales. For example, at high D the qualitative crossover from low flow concentration/high counterflow to high concentration/low counterflow (Fig. 3c) can be linked purely to a collapse in the value of ℓ_{ee} at low density while ℓ_{mr} remains larger than the device size (Fig. 3d,e). In other words, lowering the density leads to a ballistic-to-viscous crossover. At $D \approx 0$, in contrast (Fig. 3f–h), three regimes are visible as a function of n_e , with ballistic transport at high $|n_e|$ separated from a narrow region of diffusive transport near the CNP by at least one regime of viscous transport at low hole density.

We note that transport regimes are not sharply bounded, with transitions instead being described by crossover-like behavior. Thus, even though we clearly observe deeply ballistic, hydrodynamic, and diffusive regimes, any definition of their boundaries is subject to some degree of arbitrariness. Based on the characteristic device size of $w \sim d \sim 1 \mu\text{m}$, we define two thresholds of 100 nm and $2 \mu\text{m}$ (marked in Fig. 3d,e,g,h). The ballistic regime is defined as where the entire confidence interval (obtained via the RMSD) for $\ell_{\text{mr}} > 2 \mu\text{m}$ while that for $\ell_{\text{ee}} > 100$ nm. The hydrodynamic regime is defined similarly, for $\ell_{\text{mr}} > 2 \mu\text{m}$ and $\ell_{\text{ee}} < 100$ nm, while for the diffusive regime $\ell_{\text{mr}} < 2 \mu\text{m}$. Applying these criteria to the experimentally determined ℓ_{mr} and ℓ_{ee} yields ballistic, hydrodynamic, and diffusive regions shown in Fig. 3i (here darker shading indicates regions of higher confidence based on the RMSD from the model fit). Regions rendered in gray indicate crossovers where a relevant scattering length is within our confidence interval of the sample size.

The hydrodynamic regime coincides with the large- m^* region of Fig. 1c. Over much of this regime, our semiclassical Boltzmann fit gives $\ell_{\text{ee}} \lesssim 50$ nm, comparable to the Fermi wavelength $\lambda_F = 2\sqrt{\pi}/|n_e|$ at low densities; in other words, electrons scatter off of each other on a length scale comparable to their separation. This is the outer limit of the validity of the semiclassical approximation that underlies Boltzmann transport, and implies

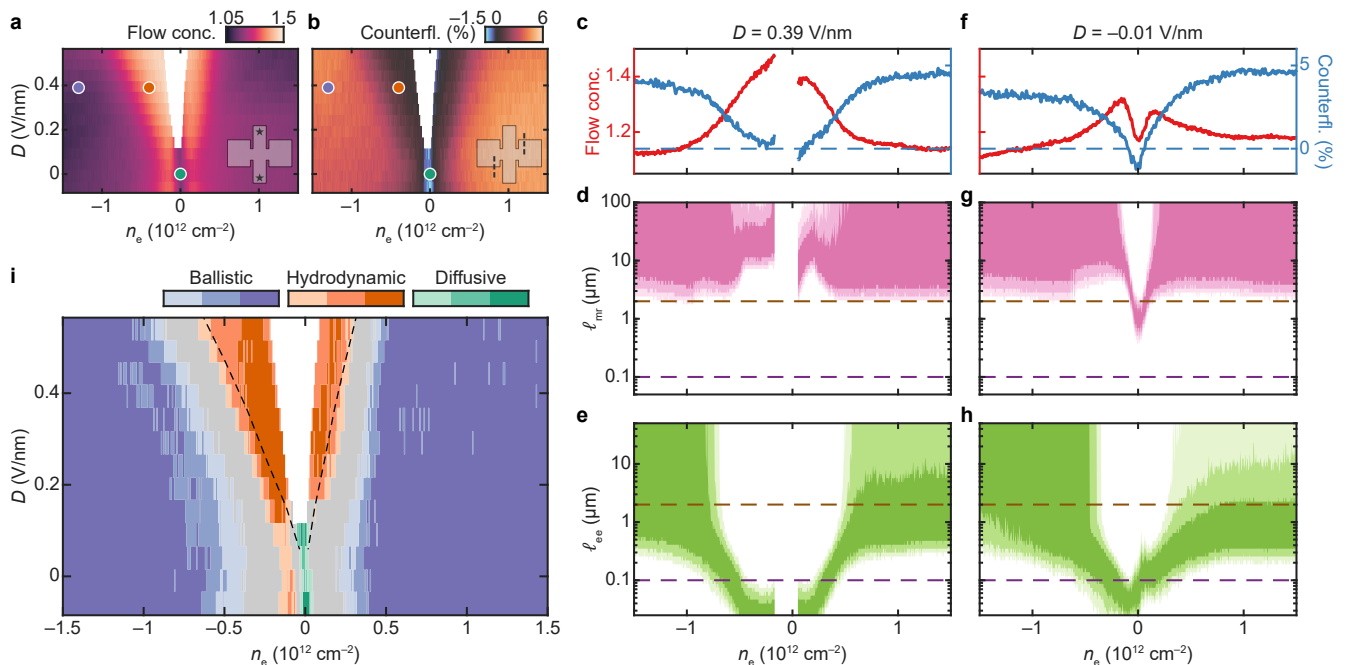


FIG. 3. **Transport regime phase diagram.** **a**, Flow concentration $J_y(x=0)/J_0$ and **b**, Counterflow $I_x(|x|=1.3\mu\text{m})/I_0$ (see main text) as a function of n_e and D . Dots represent parameters of measurements presented in Fig. 2. **c**, Flow concentration and counterflow as a function of n_e at $D = 0.39\text{ V/nm}$. **d**, Fitting ranges for ℓ_{mr} and **e**, ℓ_{ee} for the data in panel **c**. The dark, intermediate, and light shaded regions in panels **d** and **e** denote ranges where the normalized RMSD is less than 1.1, 1.2, and 1.3, respectively. Dashed lines denote 100 nm and $2\mu\text{m}$. **f**, Flow concentration and counterflow as a function of n_e at $D = -0.01\text{ V/nm}$. **g**, Fitting ranges for ℓ_{mr} and **h**, ℓ_{ee} for the data in panel **f**. **i**, Combined phase diagram indicating transport regimes. Blue represents the ballistic regime where $\min \ell_{\text{mr}} > 2\mu\text{m}$ and $\min \ell_{\text{ee}} > 100\text{ nm}$. Orange represents the hydrodynamic regime where $\min \ell_{\text{mr}} > 2\mu\text{m}$ and $\max \ell_{\text{ee}} < 100\text{ nm}$. Green represents the diffusive regime where $\max \ell_{\text{mr}} < 2\mu\text{m}$. Different shadings correspond to confidence intervals of normalized RMSD $< 1.1, 1.2, 1.3$ and gray regions indicate regime crossovers. Dashed lines delimit the extent of the regime of fluctuating magnetic moments and negative dR/dT reported in [32].

that transport is hydrodynamic on the smallest allowable length scales. Phenomenologically, our finding also implies that the negative dR/dT observed in bulk transport measurements of rhombohedral multilayers[32, 33] indeed arises from the Gurzhi effect, with the temperature-dependent viscosity dominating the resistance behavior for a finite-width channel. One implication of this finding is that if samples can be fabricated with dimensions considerably larger than the Gurzhi length, this resistance effect should weaken.

Previous thermodynamic measurements at similar values of T , n_e and D have revealed a “local moment” entropy associated with isospin fluctuations[32]; the magnitude of this entropy implies an isospin correlation length that is also comparable to λ_F . Gate-biased bilayer graphene (and presumably other rhombohedral multilayers) is thus in a nearly classical liquid state in which both the electron–electron scattering and isospin correlations are as short-range as possible given the particle density. The short ℓ_{ee} implies that the state is above the coherence temperature of the Fermi liquid. At the same time, our $T \approx 2\text{ K}$ is well below the bare energy scales set by the Fermi and interaction energies, which are both in

the few-meV range; these determine the effective Debye temperature for the electrons, defined as the frequency with which particles vibrate in the cage formed by their neighbors. The phase studied here may thus microscopically be a “semiquantum liquid” [39] in which the carrier dynamics are dominated by configurational changes between states with solid-like short-range correlations.

IMAGING NONLINEAR TRANSPORT

Our superconducting sensor puts an upper bound on the equilibrium temperature of the experimental setup, and all of the data presented above are acquired at a cryostat temperature of 1.7 K. However, it is well known that the weakness of electron–phonon coupling in graphene allows the electron temperature to be much higher than the lattice temperature, particularly under large current drive[40–42]. In our imaging experiment, the onset of such a nonlinearity is expected to manifest as a change in the microscopic current distribution. Indeed, for the analysis of the 1.7 K transport regimes of Figs. 2, 3, we take pains to measure with sufficiently small current that

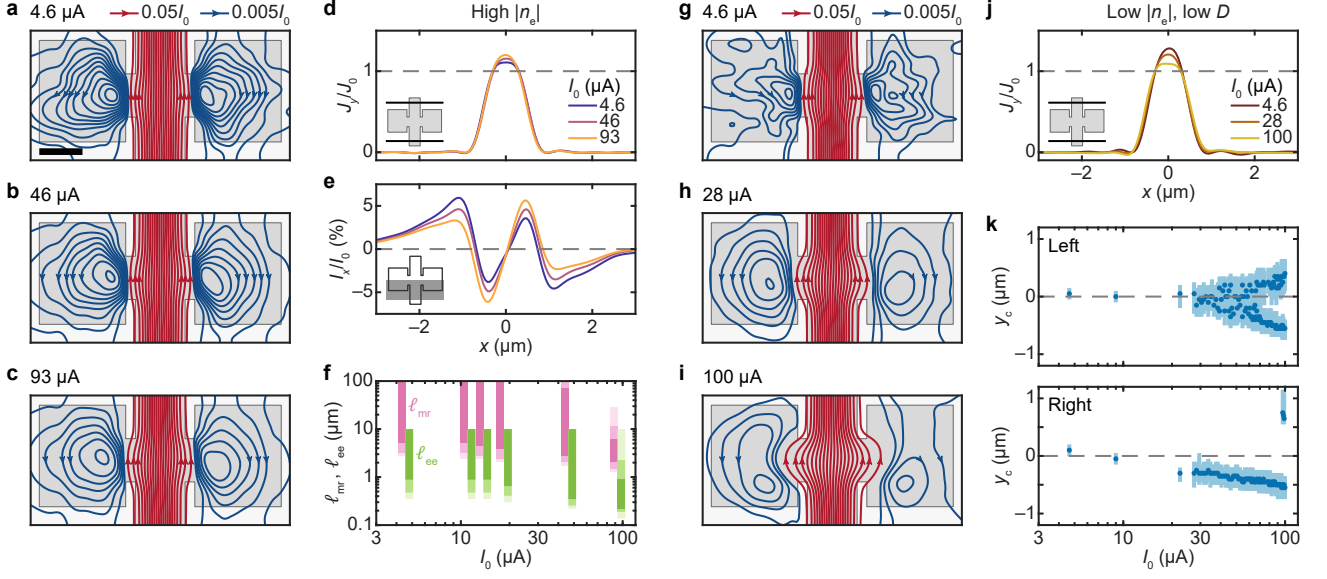


FIG. 4. **Visualizing current-driven nonlinearities.** **a**, Current streamlines for $n_e = -1.5 \times 10^{12} \text{ cm}^{-2}$ and $D = 0.39 \text{ V/nm}$ for $I_0 = 4.6 \text{ } \mu\text{A}$, **b**, $I_0 = 46 \text{ } \mu\text{A}$, and **c**, $I_0 = 93 \text{ } \mu\text{A}$. Scale bar: $1 \text{ } \mu\text{m}$. **d**, $J_y(x, \pm 2 \text{ } \mu\text{m})/J_0$ for the data in panels a, b and c. **e**, $I_x(x)/I_0$ for the data in panels a, b and c. **f**, Fitting ranges for ℓ_{mr} and ℓ_{ee} as a function of I_0 . Shadings represent confidence intervals of normalized RMSD $< 1.1, 1.2, 1.3$. **g**, Current streamlines for $n_e = -0.25 \times 10^{12} \text{ cm}^{-2}$ and $D = 0 \text{ V/nm}$ for $I_0 = 4.6 \text{ } \mu\text{A}$, **h**, $I_0 = 28 \text{ } \mu\text{A}$, and **i**, $I_0 = 100 \text{ } \mu\text{A}$. **j**, $J_y(x, \pm 2 \text{ } \mu\text{m})/J_0$ for the data in panels g, h and i. **k**, The vortex center position(s), y_c , for the left and right chambers as a function of I_0 (see Methods). $y = 0$ denotes the horizontal mirror axis of the device.

the flow profile is observed to be independent of the current amplitude. More generally, however, heating of the electron system is expected to strongly favor hydrodynamic transport, as it reduces ℓ_{ee} but may have a diminished effect on ℓ_{mr} if the phonon bath remains cold. This effect is exemplified in the current-driven evolution of the flow profile at $n_e = -1.5 \times 10^{12} \text{ cm}^{-2}$ and $D = 0.39 \text{ V/nm}$ where transport is deep in the ballistic regime at the lowest applied currents. As I_0 grows from 4.6 to $93 \text{ } \mu\text{A}$ (Fig. 4a–c), the channel current profile $J_y(x)/J_0$ increases in concentration (Fig. 4d), whereas $I_x(x)/I_0$ in the chambers gradually decreases (Fig. 4e). Current streamline plots show sparser loops for higher I_0 , indicating weakening of the vortical flow. Fitting $J_y(x)$ and $I_x(x)$ curves to the Boltzmann model (Fig. 4f) reveals a gradually decreasing ℓ_{ee} , from $\ell_{\text{ee}} \gtrsim 1 \text{ } \mu\text{m}$ to $\ell_{\text{ee}} \approx 500 \text{ nm}$, while ℓ_{mr} remains larger than the device size (see also Extended Data Fig. 6). This incipient ballistic-to-viscous crossover resembles previous experiments in light-electron graphene systems that rely on elevated equilibrium temperatures to achieve hydrodynamic regimes[2, 5], suggesting a quasi-equilibrium picture in which the temperature of the electron gas is uniformly raised due to the dissipation of the applied current.

We also observe high-current effects that go beyond the phenomenological Boltzmann model. This is demonstrated in Fig. 4g–i, where we plot current streamlines at $n_e = -0.25 \times 10^{12} \text{ cm}^{-2}$ and $D = 0 \text{ V/nm}$ for several

values of I_0 . Here, the low-current transport is within the ballistic-to-viscous crossover regime, showing both elevated flow concentration in the channel and vortical flow in the chambers. Increasing I_0 to $100 \text{ } \mu\text{A}$ causes a reduction in the channel flow concentration (Fig. 4j), suggesting a possible crossover to diffusive transport. This is consistent with some heating of the phonon bath in addition to an elevated electron temperature. However, the spatial distribution of current is qualitatively inconsistent with the Boltzmann model. Most strikingly, the vortex centers are driven away from the central horizontal axis of the device (Fig. 4k). This is accompanied by a gradual penetration of the central channel flow through the constrictions and into the chambers, which drives the vortical flow into a crescent shape (see Extended Data Video 1).

Throughout the available parameter range in the Boltzmann model spanned by ℓ_{mr} and ℓ_{ee} , vortices are always quasi-circular and on the central axis (see Extended Data Fig. 7), contrasting with the observations at high current. The breakdown of the model may have several origins. One naive possibility is a nonlinear hydrodynamic effect associated with large current flow. Within a purely hydrodynamic theory, the emergence of nonlinearities such as turbulence is parameterized by the Reynolds number $\text{Re} = \frac{4v}{v_F} \frac{L}{\ell_{\text{ee}}}$, where v is the drift velocity and v_F is the Fermi velocity. Taking an effective mass of $m^* \approx 0.05m_e$ at $\Delta_U = 0$, this gives $\text{Re} \approx 40\text{--}50$ for the

highest currents—far short of the onset of turbulence in typical fluid flows. Alternatively, the phenomenological nature of the Boltzmann model may ignore too many features of the intricate low-energy band structure of R2G to be quantitatively accurate, which may manifest most strongly at high currents. In particular, a large current drive may lead to spatially dependent shifts in the chemical potential which may alter the flow pattern. Both the density of states and the anisotropy of the Fermi surfaces are chemical potential dependent in R2G but these effects are ignored in our Boltzmann model where the band structure is assumed to be that of a single parabolically dispersing band. Finally, the equilibrium temperature profile (for either the electrons, phonons, or both) can be spatially nonuniform, allowing a higher temperature in the channel as compared to the chambers.

Microscopic theoretical modeling may elucidate the origin of these effects, and help harness them for functional device applications based on nonlinear viscous transport[43]. More broadly, effective mass tuning of ℓ_{ee} into a deeply hydrodynamic regime opens a new avenue to pursuing extreme hydrodynamic effects in electron fluids. For example, future experiments in rhombohedral multilayers of higher layer number (where m^* can be even larger than in R2G) combined with custom geometries may access regimes of Reynolds number compatible with turbulent flow. The highly anisotropic Fermi surfaces in these devices may also facilitate the observation of anisotropic viscosity in the hydrodynamic regime[44, 45], a unique feature of electron hydrodynamics which has not been explored experimentally. Finally, the scheme for mapping microscopic transport regimes may shed light on the wealth of correlated electron physics now available in ultraclean crystalline two-dimensional material systems.

* These authors contributed equally.

† andrea@physics.ucsb.edu

- [1] Gurzhi, R. N. Hydrodynamic effects in solids at low temperature. *Soviet Physics Uspekhi* **11**, 255 (1968).
- [2] Bandurin, D. A. *et al.* Negative local resistance caused by viscous electron backflow in graphene. *Science* **351**, 1055–1058 (2016).
- [3] Krishna Kumar, R. *et al.* Superballistic flow of viscous electron fluid through graphene constrictions. *Nature Physics* **13**, 1182–1185 (2017).
- [4] Bandurin, D. A. *et al.* Fluidity onset in graphene. *Nature Communications* **9**, 4533 (2018).
- [5] Berdyugin, A. I. *et al.* Measuring hall viscosity of graphene’s electron fluid. *Science* **364**, 162–165 (2019).
- [6] Sulpizio, J. A. *et al.* Visualizing poiseuille flow of hydrodynamic electrons. *Nature* **576**, 75–79 (2019).
- [7] Ku, M. J. H. *et al.* Imaging viscous flow of the dirac fluid in graphene. *Nature* **583**, 537–541 (2020).
- [8] Kim, M. *et al.* Control of electron-electron interaction in graphene by proximity screening. *Nature Communications* **11**, 2339 (2020).
- [9] Jenkins, A. *et al.* Imaging the breakdown of ohmic transport in graphene. *Phys. Rev. Lett.* **129**, 087701 (2022).
- [10] Kumar, C. *et al.* Imaging hydrodynamic electrons flowing without landauer–sharvin resistance. *Nature* **609**, 276–281 (2022).
- [11] Huang, W. *et al.* Electronic poiseuille flow in hexagonal boron nitride encapsulated graphene field effect transistors. *Phys. Rev. Res.* **5**, 023075 (2023).
- [12] Krebs, Z. J. *et al.* Imaging the breaking of electrostatic dams in graphene for ballistic and viscous fluids. *Science* **379**, 671–676 (2023).
- [13] Palm, M. L. *et al.* Observation of current whirlpools in graphene at room temperature. *Science* **384**, 465–469 (2024).
- [14] Talanov, A. *et al.* Observation of electronic viscous dissipation in graphene magneto-thermal transport (2024). URL <https://arxiv.org/abs/2406.13799>. 2406.13799.
- [15] Koshino, M. & McCann, E. Trigonal warping and berry’s phase $n\pi$ in abc-stacked multilayer graphene. *Phys. Rev. B* **80**, 165409 (2009).
- [16] Finkler, A. *et al.* Self-aligned nanoscale squid on a tip. *Nano Letters* **10**, 1046–1049 (2010).
- [17] Vasyukov, D. *et al.* A scanning superconducting quantum interference device with single electron spin sensitivity. *Nature Nanotechnology* **8**, 639–644 (2013).
- [18] Aharon-Steinberg, A. *et al.* Direct observation of vortices in an electron fluid. *Nature* **607**, 74–80 (2022).
- [19] Lucas, A. & Fong, K. C. Hydrodynamics of electrons in graphene. *Journal of Physics: Condensed Matter* **30**, 053001 (2018).
- [20] Fritz, L. & Scaffidi, T. Hydrodynamic electronic transport. *Annual Review of Condensed Matter Physics* **15**, 17–44 (2024).
- [21] Narozhny, B. N., Gornyi, I. V., Titov, M., Schütt, M. & Mirlin, A. D. Hydrodynamics in graphene: Linear-response transport. *Phys. Rev. B* **91**, 035414 (2015).
- [22] Levitov, L. & Falkovich, G. Electron viscosity, current vortices and negative nonlocal resistance in graphene. *Nature Physics* **12**, 672–676 (2016).
- [23] Giuliani, G. & Vignale, G. *Quantum Theory of the Electron Liquid* (Cambridge University Press, 2005).
- [24] Jung, J. & MacDonald, A. H. Accurate tight-binding models for the π bands of bilayer graphene. *Phys. Rev. B* **89**, 035405 (2014).
- [25] Zhou, H. *et al.* Isospin magnetism and spin-polarized superconductivity in bernal bilayer graphene. *Science* **375**, 774–778 (2022).
- [26] de la Barrera, S. C. *et al.* Cascade of isospin phase transitions in bernal-stacked bilayer graphene at zero magnetic field. *Nature Physics* **18**, 771–775 (2022).
- [27] Seiler, A. M. *et al.* Quantum cascade of correlated phases in trigonally warped bilayer graphene. *Nature* **608**, 298–302 (2022).
- [28] Zhang, Y. *et al.* Enhanced superconductivity in spin-orbit proximitized bilayer graphene. *Nature* **613**, 268–273 (2023).
- [29] Li, C. *et al.* Tunable superconductivity in electron- and hole-doped bernal bilayer graphene. *Nature* **631**, 300–306 (2024).
- [30] Holleis, L. *et al.* Nematicity and orbital depairing in superconducting bernal bilayer graphene. *Nature Physics* **21**, 444–450 (2025).

- [31] Zhang, Y. *et al.* Twist-programmable superconductivity in spin-orbit-coupled bilayer graphene. *Nature* **641**, 625–631 (2025).
- [32] Holleis, L. *et al.* Fluctuating magnetism and pomeranchuk effect in multilayer graphene. *Nature* **640**, 355–360 (2025).
- [33] Seiler, A. M. *et al.* Interaction-driven quasi-insulating ground states of gapped electron-doped bilayer graphene. *Phys. Rev. Lett.* **133**, 066301 (2024).
- [34] Andreev, A. V., Kivelson, S. A. & Spivak, B. Hydrodynamic description of transport in strongly correlated electron systems. *Phys. Rev. Lett.* **106**, 256804 (2011).
- [35] Lucas, A. & Hartnoll, S. A. Kinetic theory of transport for inhomogeneous electron fluids. *Phys. Rev. B* **97**, 045105 (2018).
- [36] Colvin, R. V., Legvold, S. & Spedding, F. H. Electrical resistivity of the heavy rare-earth metals. *Phys. Rev.* **120**, 741–745 (1960).
- [37] Fisher, M. E. & Langer, J. S. Resistive anomalies at magnetic critical points. *Phys. Rev. Lett.* **20**, 665–668 (1968).
- [38] Torre, I., Tomadin, A., Geim, A. K. & Polini, M. Non-local transport and the hydrodynamic shear viscosity in graphene. *Phys. Rev. B* **92**, 165433 (2015).
- [39] Andreev, A. F. & Kosevich, Y. A. Kinetic phenomena in semiquantum liquids. *Zh. Eksp. Teor. Fiz* **77**, 2518–2523 (1979).
- [40] Meric, I. *et al.* Current saturation in zero-bandgap, top-gated graphene field-effect transistors. *Nature Nanotechnology* **3**, 654–659 (2008).
- [41] Massicotte, M., Soavi, G., Principi, A. & Tielrooij, K.-J. Hot carriers in graphene – fundamentals and applications. *Nanoscale* **13**, 8376–8411 (2021).
- [42] Srivastav, S. K. *et al.* Revealing electron-lattice decoupling by peltier thermometry and nanoscale thermal imaging in graphene (2025). URL <https://arxiv.org/abs/2506.21523>. 2506.21523.
- [43] Geurs, J. *et al.* Rectification by hydrodynamic flow in an encapsulated graphene tesla valve (2020). URL <https://arxiv.org/abs/2008.04862>. 2008.04862.
- [44] Cook, C. Q. & Lucas, A. Electron hydrodynamics with a polygonal fermi surface. *Phys. Rev. B* **99**, 235148 (2019).
- [45] Varnavides, G., Jermyn, A. S., Anikeeva, P., Felser, C. & Narang, P. Electron hydrodynamics in anisotropic materials. *Nature Communications* **11**, 4710 (2020).
- [46] Redekop, E. *et al.* Direct magnetic imaging of fractional chern insulators in twisted mote2. *Nature* **635**, 584–589 (2024).
- [47] Huber, M. *et al.* Dc squid series array amplifiers with 120 mhz bandwidth. *IEEE Transactions on Applied Superconductivity* (2001).
- [48] Feldmann, D. M. Resolution of two-dimensional currents in superconductors from a two-dimensional magnetic field measurement by the method of regularization. *Phys. Rev. B* **69**, 144515 (2004).
- [49] Meltzer, A. Y., Levin, E. & Zeldov, E. Direct reconstruction of two-dimensional currents in thin films from magnetic-field measurements. *Phys. Rev. Appl.* **8**, 064030 (2017).
- [50] Bhatnagar, P. L., Gross, E. P. & Krook, M. A model for collision processes in gases. i. small amplitude processes in charged and neutral one-component systems. *Physical Review* **94**, 511–525 (1954).
- [51] Mendl, C. B. & Lucas, A. Dyakonov-shur instability across the ballistic-to-hydrodynamic crossover. *Applied Physics Letters* **112**, 124101 (2018).
- [52] Ledwith, P., Guo, H., Shytov, A. & Levitov, L. Tomographic dynamics and scale-dependent viscosity in 2d electron systems. *Physical Review Letters* **123**, 116601 (2019).
- [53] Farrell, J. H. & Lucas, A. Simple devices that distinguish viscous, ballistic, and diffusive transport. *to appear* (2026).
- [54] Farrell, J. H. FermiHarmonics: Linearized 2d fermi-liquid boltzmann transport on unstructured meshes. *Zenodo* (2026).
- [55] Ranocha, H. *et al.* Adaptive numerical simulations with Trixi.jl: A case study of Julia for scientific computing. *Proceedings of the JuliaCon Conferences* **1**, 77 (2022).
- [56] Schlottke-Lakemper, M., Winters, A. R., Ranocha, H. & Gassner, G. J. A purely hyperbolic discontinuous Galerkin approach for self-gravitating gas dynamics. *Journal of Computational Physics* **442**, 110467 (2021).

METHODS

Sample fabrication

Dual-gated R2G was fabricated through van der Waals stacking of bilayer graphene, hexagonal boron nitride (hBN) dielectric layers, and few-layer graphite gate plates. The flakes were prepared by mechanical exfoliation on Si/SiO₂ substrates. To begin the stacking process, graphite exfoliated on polydimethylsiloxane (PDMS) was dropped onto hBN. Poly(bisphenol A carbonate) (PC) film was then used to pick up the graphite-hBN pair as well as subsequent graphene, hBN, and graphite layers. The finished stack was dropped onto an Si/SiO₂ substrate, and the PC film was washed off with N-methylpyrrolidone.

Electron-beam lithography (EBL) was used to define a contact electrode pattern in a PMMA A8 950K resist mask. A CHF₃/O₂ ICP-RIE plasma etch followed by electron-beam deposition of chromium/palladium/gold was used to make edge contacts to individual layers of the stack. Then, an etch mask was defined via EBL of a PMMA A4 495K/A2 950K bilayer resist followed by electron-beam evaporation of aluminum. The rectangular lateral chambers were defined using a second, separate aluminum mask in order to avoid EBL proximity effects that would distort the intended device geometry. All EBL processes were performed using a scanning electron microscope equipped with a Nanometer Pattern Generation System. After the deposition of both aluminum masks, the stack was etched using a CHF₃/O₂ ICP-RIE plasma etch. Finally, the sample was immersed in an AZ300MIF solution for 20 minutes to remove the aluminum.

nSOT measurements

Local magnetometry measurements were performed in a liquid helium cryostat at a base temperature of 1.7 K using a superconducting quantum interference device on the apex of a quartz tube (nanoSQUID-on-tip, nSOT). The probe was fabricated following established protocols[16, 17, 46]. A quartz micropipette with an inner diameter of 0.5 mm was pulled under laser heating into a sharp tip with an apex diameter of ~ 160 nm. 10 nm titanium/50 nm gold side contacts were deposited via electron beam evaporation, followed by an additional 10 nm titanium/15 nm platinum strip positioned at ~ 0.5 mm from the tip apex that forms a shunt resistor of $\sim 3 \Omega$. The contact pads were subsequently coated with a thick layer of indium solder to ensure reliable electrical contact at cryogenic temperatures. Finally, indium was deposited onto the tip in a home-built thermal evaporator held at $T < 20$ K: first at 110° relative to the tip axis to cover the two opposing contacts (45–60 nm), and then head-on (40–50 nm). This sequence produced a

uniform, low-grain-size superconducting film interposed with two Dayem-bridge-type Josephson junctions. The resulting sensor exhibited a magnetic field sensitivity of $\sim 10 \text{ nT Hz}^{-1/2}$, corresponding to a flux sensitivity of $\sim 200 \text{ n}\Phi_0 \text{ Hz}^{-1/2}$ where $\Phi_0 = h/2e$ is the superconducting magnetic flux quantum (the signal was read out using a series SQUID array amplifier[47] in a flux-locked loop).

During measurements, the sample was biased in a quasi-constant-current configuration (i.e., under a constant bias voltage through a series resistor of 10–100 k Ω). Bias was applied symmetrically from two sides to provide virtual grounding in the center of the active region. True square wave current ($f = 1477.7 \text{ Hz}$) was employed to maintain constant power dissipation and thereby suppress parasitic thermal response of nSOT. Application of a few μA of current, however, became difficult when R2G turned highly resistive under very low $|n_e|$ and high D due to slow charging and parasitic capacitive signal; this regime is accordingly excluded from the phase diagrams of Fig. 3.

Measurement conditions for presented data

nSOT bias field (mT)	nSOT transfer function (V/T)		nSOT scan height (nm)
29.3	30–30.8		135

Data	Bias voltage (V)	Series resistor (k Ω)	I_0 (μA)
Figure 2a,b, Extended Data Fig. 2a–d	0.5	100	4.6
Figure 2c,d, Extended Data Fig. 2e–h	0.5	100	4.5
Figure 2e,f, Extended Data Fig. 2i–l	0.5	100	4.5
Figure 3a,b,c,f	0.1	10	3.2–6.9
Figure 4a–c, Extended Data Fig. 3a,b	0.5–10	100	4.6–93
Figure 4g	0.5	100	4.6
Figure 4h,i	0.52–2.0	10	28–100

Reconstruction of current density and streamlines

Overview. Two-dimensional (2d) current density components $J_x(x, y)$ and $J_y(x, y)$, as well as the associated streamlines, were reconstructed from the measured fringe magnetic field $B(x, y)$ using a Fourier-space inversion algorithm[48, 49]. The streamlines correspond to contours of the stream function $g(x, y)$, defined such that

$$\nabla \times (g(x, y)\hat{z}) = \mathbf{J}(x, y). \quad (3)$$

The difference in g between two streamlines represents the net current flowing between them. The scalar field $g(x, y)$ and the vector $\mathbf{J}(x, y)$ therefore contain equivalent information (up to an additive constant) and can be independently inverted from the measured $B(x, y)$.

Forward model. In Fourier space, the forward kernel propagating g to the measured B field is

$$\hat{K}_g(k_x, k_y) = \frac{\mu_0}{2} \left(\sqrt{k_x^2 + k_y^2} - ik_x \tan \theta \cos \varphi - ik_y \tan \theta \sin \varphi \right) e^{-\sqrt{k_x^2 + k_y^2} h}, \quad (4)$$

while the kernels connecting \mathbf{J} to B are

$$\hat{K}_x(k_x, k_y) = -\frac{\mu_0}{2} \left(i \frac{k_y}{\sqrt{k_x^2 + k_y^2}} + \tan \theta \sin \varphi \right) e^{-\sqrt{k_x^2 + k_y^2} h}, \quad (5a)$$

$$\hat{K}_y(k_x, k_y) = \frac{\mu_0}{2} \left(i \frac{k_x}{\sqrt{k_x^2 + k_y^2}} + \tan \theta \cos \varphi \right) e^{-\sqrt{k_x^2 + k_y^2} h}. \quad (5b)$$

Here h is the nSOT scan height and θ and φ are tilt angles of the nSOT such that $B = B_z + \tan \theta (B_x \cos \varphi + B_y \sin \varphi)$. In our experiment a small unintentional tilt was present; a choice of $\theta = 7.5^\circ$ and $\varphi = 0^\circ$ provided good agreement between measured and simulated signals. To account for finite nSOT size, all kernels were further multiplied by the point spread function

$$\hat{f}(k_x, k_y) = \frac{2\mathcal{J}_1 \left(\sqrt{k_x^2 + k_y^2} r \right)}{\sqrt{k_x^2 + k_y^2} r}, \quad (6)$$

where \mathcal{J}_1 is the first-order Bessel function and r is the effective nSOT radius.

Inverse problem and regularization. The quantities $\hat{g}(k_x, k_y)$, $\hat{J}_x(k_x, k_y)$ and $\hat{J}_y(k_x, k_y)$ in Fourier space were obtained through Tikhonov regularization with a Laplacian operator,

$$\hat{g}(k_x, k_y) = \frac{\hat{K}_g^*(k_x, k_y) \hat{B}(k_x, k_y)}{\left| \hat{K}_g(k_x, k_y) \right|^2 + \lambda_g (k_x^2 + k_y^2)^2}, \quad (7)$$

and

$$\hat{J}_x(k_x, k_y) = \frac{\hat{K}_x^*(k_x, k_y) \hat{B}(k_x, k_y)}{\left| \hat{K}_x(k_x, k_y) \right|^2 + \left| \hat{K}_y(k_x, k_y) \right|^2 + \lambda_J (k_x^2 + k_y^2)^2}, \quad (8a)$$

$$\hat{J}_y(k_x, k_y) = \frac{\hat{K}_y^*(k_x, k_y) \hat{B}(k_x, k_y)}{\left| \hat{K}_x(k_x, k_y) \right|^2 + \left| \hat{K}_y(k_x, k_y) \right|^2 + \lambda_J (k_x^2 + k_y^2)^2}. \quad (8b)$$

Here λ_g and λ_J are regularization parameters that control the tradeoff between noise amplification (for small λ) and oversmoothing (for large λ). Optimal values for our datasets are $\lambda_g = 5 \times 10^{-5} \text{ T}^2 \mu\text{m}^4 \text{ A}^{-2}$ and $\lambda_J = 5 \times 10^{-6} \text{ T}^2 \mu\text{m}^6 \text{ A}^{-2}$.

Padding and background correction. Accurate Fourier-space inversion requires $B(x, y)$ to be defined over the full 2d plane. Because experimental data are finite in extent, we padded the measured $B(x, y)$ beyond the scan window under specific boundary assumptions. Two different schemes, *Replication*—extending the edge values outward, and *Reflection*—mirroring the data across the boundary, were found to produce less than 3% difference in normalized $\mathbf{J}(x, y)$ and $g(x, y)$.

A further correction addresses the unconstrained $\mathbf{k} = 0$ component of the inversion (where the kernels either vanish or are ill-defined), which can otherwise yield unphysical net currents across the scan region. We subtracted the mean value of $J_y(x, y)$ over the area outside the device boundary but within the measurement window, en-

suring that the average background current vanishes. In some cases, we additionally subtracted a parabolic background fitted to J_y to remove residual slow-varying artifacts. The stream function $g(x, y)$ was then shifted accordingly to maintain Eq. (3).

Simplified 1d reconstruction

The above procedures yield full 2d maps of $\mathbf{J}(x, y)$ and $g(x, y)$ but require complete spatial maps of $B(x, y)$ as input. For flow concentration and counterflow plots in Fig. 3, we instead adopted a more efficient approach where $J_y(x, \pm y_0)$ and $I_x(x)$ are derived from magnetic field data along a one-dimensional (1d) trajectory. $J_y(x, \pm y_0)$ can be directly reconstructed from $B(x, \pm y_0)$, since these regions are far away from the lateral chambers and therefore translationally invariant in y (i.e., $k_y = 0$);

here, the inversion reduces to

$$\hat{J}_y(k_x) = \frac{\hat{K}_y^*(k_x, 0)\hat{B}(k_x)}{\left|\hat{K}_x(k_x, 0)\right|^2 + \left|\hat{K}_y(k_x, 0)\right|^2 + \lambda_J k_x^4}. \quad (9)$$

Estimating $I(x)$ is more subtle. This quantity can be rewritten as

$$I(x) \equiv \Delta g(x) = g(x, 0) - \frac{g(x, -y_0) + g(x, y_0)}{2}, \quad (10)$$

which bears similarity to the corresponding field difference $\Delta B(x) = B(x, 0) - \frac{B(x, -y_0) + B(x, y_0)}{2}$. In general, $\Delta g(x)$ and $\Delta B(x)$ are not uniquely connected, since the full kernel (4) relating $g(x, y)$ to $B(x, y)$ depends on the

transverse wavenumber k_y . However, the definition of $\Delta B(x)$, together with the spatial structure of $B(x, y)$, introduces a natural filter in k_y . Specifically, the effective window function suppresses long-wavelength components and peaks at finite $|k_y|$, thereby selecting a characteristic transverse wavenumber $|k_y| \approx 2\pi/l_y$ where l_y denotes the y scale of the chambers. Within this approximation, the inversion takes the form

$$\hat{\Delta g}(k_x) = \frac{\hat{K}_g^*(k_x)\hat{\Delta B}(k_x)}{\left|\hat{K}_g(k_x)\right|^2 + \lambda_g k_x^4}, \quad (11)$$

with an effective 1d kernel

$$\hat{K}_g(k_x) = \frac{\mu_0}{2} \left(\sqrt{k_x^2 + \left(\frac{2\pi}{l_y}\right)^2} - ik_x \tan \theta \cos \varphi \right) e^{-\sqrt{k_x^2 + \left(\frac{2\pi}{l_y}\right)^2} h}. \quad (12)$$

Here the ik_y term in the original 2d kernel is dropped since the filtering preserves the $\pm k_y$ components symmetrically. Extended Data Figure 8 compares $\hat{\Delta g}(x)$ reconstructed using this 1d approximation ($l_y = 3\mu\text{m}$) to the full 2d result, showing good agreement and validating the simplified procedure.

Numerical simulations

As a minimal model describing the device across the ballistic, hydrodynamic, and diffusive regimes, we consider a toy kinetic theory of one species of fermions in 2d with isotropic dispersion relation $\epsilon(|\mathbf{k}|)$, with a circular Fermi surface corresponding to $\epsilon_F = \mu_0 = \epsilon(|\mathbf{k}|)$. We work in linear response and assume $T \ll T_F$, so that the single particle distribution function $f(\mathbf{x}, \mathbf{k})$ is approxi-

mately

$$f(\mathbf{x}, \mathbf{k}) = \Theta(\mu_0 - \epsilon(\mathbf{k})) - \phi(\mathbf{x}, \mathbf{k})\delta(\mu_0 - \epsilon(\mathbf{k})), \quad (13)$$

where $\phi(\mathbf{x}, \mathbf{k})$ parametrizes the linear-response deviation from equilibrium of the distribution function, Θ is the Heaviside step function, and δ is Dirac's delta function. It is convenient to take the momentum dependence in polar coordinates, $k_x = k \cos \theta$, $k_y = k \sin \theta$. Given Eq. (13), we may then treat ϕ as dependent only on θ , as the delta function fixes $k = k_F$ [with $\epsilon_F = \epsilon(k_F)$]. The Boltzmann transport equation for f can be rewritten in terms of ϕ as

$$\partial_t \phi + v_F (\cos \theta \partial_x + \sin \theta \partial_y) \phi = -W[\phi], \quad (14)$$

where v_F is the Fermi velocity (in general, dependent on the electronic chemical potential μ_0) and $W[\phi]$ is the collision integral describing the interaction of particles with their environment or each other. We have also assumed the absence of external forcing on the electrons.

Assuming ϕ is small, we may linearize the equations around equilibrium $\phi = 0$. In this regime, Eq. (14) admits a natural Fourier decomposition

$$\phi = \frac{a_0(\mathbf{x}, t)}{2} + \sum_{m=1}^{\infty} (a_m(\mathbf{x}, t) \cos(m\theta)) + b_m(\mathbf{x}, t) \sin(m\theta)). \quad (15)$$

For the collision matrix, we may use rotational symmetry to restrict the form of $W[\phi]$ as

$$W[\phi] = v_F l_0^{-1} \frac{a_0(\mathbf{x}, t)}{2} + \sum_{m=1}^{\infty} v_F l_m^{-1} (a_m(\mathbf{x}, t) \cos(m\theta)) + b_m(\mathbf{x}, t) \sin(m\theta)), \quad (16)$$

where l_n represents a mean free path for the n^{th} Fourier harmonic. In steady state, Eq. (14) becomes an infinite set of coupled partial differential equations

$$\partial_x a_1 + \partial_y b_1 = -l_0^{-1} a_0, \quad (17a)$$

$$\frac{1}{2} [\partial_x (a_{n+1} + a_{n-1}) + \partial_y (b_{n+1} - b_{n-1})] = -l_n^{-1} a_n, \quad n \geq 1, \quad (17b)$$

$$\frac{1}{2} [\partial_x (b_{n+1} + b_{n-1}) - \partial_y (a_{n+1} - a_{n-1})] = -l_n^{-1} b_n, \quad n \geq 1. \quad (17c)$$

Here $b_0 \equiv 0$. We further adopt a two-time collision integral with ℓ_{mr} representing the mean free path between momentum-relaxing collisions and ℓ_{ee} that between momentum-conserving collisions, namely

$$l_0^{-1} = 0, \quad (18a)$$

$$l_1^{-1} = \ell_{\text{mr}}^{-1}, \quad (18b)$$

$$l_n^{-1} = \ell_{\text{mr}}^{-1} + \ell_{\text{ee}}^{-1}, \quad n \geq 2. \quad (18c)$$

This corresponds to a linearized BGK model[50, 51]. We note that considering separate l_n for even and odd n would be straightforward and capture tomographic physics expected to be relevant for 2d electron liquids[52], but we find that two fit parameters are already sufficient to quantitatively model the present experiment.

We solve Eqs. (17) numerically[53, 54] using discontinuous Galerkin spectral element methods (DGSEM) as implemented in the `Trixi.jl` package for the Julia programming language[55, 56]. In particular, the solution is spatially reconstructed as a degree 4 polynomial within each cell of an unstructured quadrilateral mesh with average grid size $dx = dy = 100$ nm. The high-order reconstruction allows us to obtain accurate numerical solutions which capture the complex flows in the experimental geometry, despite the relatively coarse mesh. The Fourier series (15) are truncated at $n = n_{\text{max}}$, and we have run simulations with a high $n_{\text{max}} = 50$ to quantitatively capture ballistic physics. The surface flux is local Lax–Friedrichs. To find the stationary solution, we integrate forward Eq. (14) in time using an explicit Carpenter–Kennedy Runge–Kutta scheme until convergence to a time-independent solution is reached. Convergence is determined by the maximum residual, i.e., the ∞ -norm of the time derivative $\left\| \frac{d\phi}{dt} \right\|_{\infty} \equiv \max \left| \frac{d\phi}{dt} \right|$.

We have considered two types of boundary condition on the wall of the device, namely diffuse scattering and specular reflection. In either case, we must constrain only degrees of freedom (particles) that are *incoming* to the domain. In the diffuse case, we choose a_n and b_n at the walls such that (at appropriately discretized angles) the value of $\phi(\theta)$ is uniform at every angle θ corresponding to a particle propagating away from the boundary. This constant value is chosen to ensure that no particles are emitted or absorbed by the boundary. In the case of specular reflection, the incoming degrees of freedom are

instead constrained to satisfy $\phi(\theta) = \phi(\pi - \theta)$, which constrains the distribution at an outgoing angle in terms of an incoming angle.

On the source and drain contacts, we also constrain only the angles corresponding to particles entering the domain from the boundary. In this case, we again pick a_n and b_n such that the value of $\phi(\theta)$ is uniform at all angles corresponding to particles entering the domain, with constant value this time held *fixed* rather than chosen to guarantee zero particles injected or absorbed at the boundary. This choice models an ideal (absorbing) Ohmic contact held at a fixed potential.

Least squares fitting

The reconstructed experimental current density differs from the true distribution due to spatial filtering (finite scan height, finite nSOT size, regularization, etc.) and numerical artifacts such as ringing. In contrast, the theoretically computed current density is exact within the model assumptions. Consequently, direct comparison between experimental and theoretical $\mathbf{J}(x, y)$ or derived quantities such as $J_y(x)$ and $I_x(x)$ is often problematic. Instead, we performed fitting in the magnetic field space. Specifically, for each set of parameters ($\ell_{\text{mr}}, \ell_{\text{ee}}$), we computed theoretical $B(x, y)$ from simulated $\mathbf{J}(x, y)$ using the forward kernels (5) (i.e., Biot–Savart law), which we then compared to the measured B signal.

Equations (9), (11) have established that $J_y(x, \pm y_0)$ and $I_x(x)$ are related to $B(x, \pm y_0)$ and $\Delta B(x)$, respectively. We therefore define two per-pixel root mean square deviations (RMSDs): $\text{RMSD}(J_y)$, computed from $B(x, \pm y_0)$ over the range $-1.2 \mu\text{m} \leq x \leq 1.2 \mu\text{m}$, and $\text{RMSD}(I_x)$, computed from $\Delta B(x)$ over $-1.8 \mu\text{m} \leq x \leq 1.8 \mu\text{m}$. In both cases, the magnetic signal is normalized by $B_{\text{range}} \equiv B_{\text{max}} - B_{\text{min}}$ of the scan frame. The best-fit parameters were obtained by minimizing the (equally weighted) combined $\text{RMSD} := \sqrt{\text{RMSD}(J_y)^2 + \text{RMSD}(I_x)^2}$.

We find that $\text{RMSD}(J_y)$ and $\text{RMSD}(I_x)$ predominantly probe channel flow and vortex profiles, respectively, and that their combination is necessary in determining the exact transport regime. At the CNP, for example, $\text{RMSD}(J_y)$ is small over a broad range of ℓ_{mr} and

ℓ_{ee} (Extended Data Fig. 4a); both diffusive (green) and ballistic (purple) regimes produce a flat current profile, consistent with the experimental data (Extended Data Fig. 4b). A good fit for $I_x(x)$, however, is achieved only in the diffusive regime and not in the ballistic regime (Extended Data Fig. 4c,d). At high density, in contrast, $\text{RMSD}(I_x)$ favors instead the ballistic regime, consistent with the observed strong vortical flow (Extended Data Fig. 4g,h). Finally in the low- $|n_e|$, high- D flat band regime, $\text{RMSD}(I_x)$ allows two scenarios (Extended Data Fig. 4k,l): the hydrodynamic regime (orange), or the direct crossover between diffusive and ballistic regimes in which ℓ_{ee} remains large (blue). Here, J_y is crucial in the identification of hydrodynamic transport which alone can generate the concentrated Poiseuille flow (Extended Data Fig. 4i,j).

Visualizing fits via reconstructed current

Once optimal values of ℓ_{mr} and ℓ_{ee} are determined, we visualize best fits through “mock reconstructions” of theoretical $\mathbf{J}(x, y)$ and $g(x, y)$, obtained by applying to calculated $B(x, y)$ the identical reconstruction procedure (padding, regularization, and background correction) as used for the experimental data. Extended Data Figure 5 compares direct simulated and mock reconstructed $J_y(x, y)$ and current streamlines in the diffusive, ballistic, and hydrodynamic regimes. The reconstruction faithfully preserves all essential current features distinguishing these regimes, including flow concentration and counterflow, while reproducing the smoothing, ringing, and background artifacts characteristic of experimental results. All theoretical current plots in the main text and other Extended Data Figures employ this simulation + reconstruction procedure.

Quantifying vortex deformation

To quantify the current-driven deformation of vortical flow, we analyzed vortex center position(s), y_c , marked by local extrema of the current stream function $g(x, y)$ (maxima for counterclockwise vortices and minima for clockwise vortices). Figure 4k shows the evolution of y_c for both chambers upon increasing I_0 ; error bars are defined by $|g - g_0| < 0.001I_0$ where g_0 is the extremum value. Small values of I_0 give $y_c \approx 0$, i.e., vortices centered near the central horizontal axis of the device. Under large I_0 , in contrast, the vortical flow assumes a crescent shape with two separate centers at the top and bottom halves of the scan frame (see, for example, Fig. 4i). This behavior is found to be absent in the linearized Boltzmann model, which always features $y_c \approx 0$ in regimes of positive counterflow (Extended Data Fig. 7a,b).

ACKNOWLEDGMENTS

The authors acknowledge discussions with L.Levitov, L.I.Glazman, B.Skinner, L.Balents, E.Berg, K.G.Nazaryan, and A.Panigrahi. Experimental work at UCSB was primarily supported by the Department of Energy under Award DE-SC0020043 to A.F.Y. Additional funding for nSOT sensor and microscope development was provided by the Experimental Physics Investigator program of the Gordon and Betty Moore Foundation under Award GBMF-13801 to A.F.Y. S.K. and A.C.B.J. acknowledge support from the Gordon and Betty Moore Foundation’s EPiQS Initiative via Grant GBMF-10279. K.W. and T.T. acknowledge support from the JSPS KAKENHI (Grant Numbers 21H05233 and 23H02052), the CREST (JPMJCR24A5), JST and World Premier International Research Center Initiative (WPI), MEXT, Japan. Theoretical modeling at CU Boulder was supported by the National Science Foundation under CAREER Grant DMR-2145544. E.R. acknowledges direct support by the National Science Foundation through Enabling Quantum Leap: Convergent Accelerated Discovery Foundries for Quantum Materials Science, Engineering and Information (Q-AMASE-i) Award DMR-1906325; the work also made use of shared equipment sponsored under this award.

AUTHOR CONTRIBUTIONS

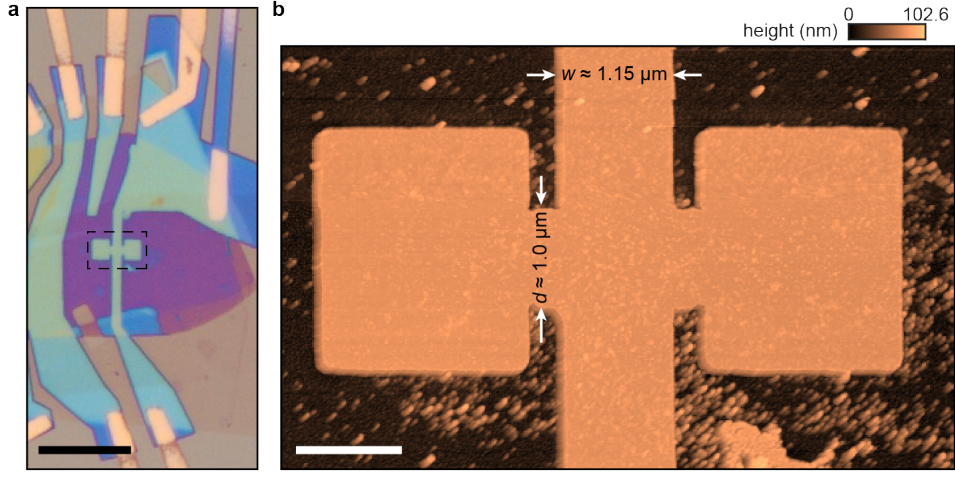
A.F.Y. conceived and supervised the project. H.S., S.K., L.H. and Y.C. designed and fabricated the device. T.T. and K.W. grew the hBN crystals. D.G. and A.K. prepared nanoSQUID-on-tip sensors. C.Z. and E.R. performed the measurements and data analysis. C.Z. optimized the current reconstruction algorithm. J.H.F. developed the numerical methods. J.H.F. and A.L. provided theoretical support. M.E.H. provided SQUID array amplifiers for nSOT readout. C.Z., E.R. and A.F.Y. wrote the paper with inputs from all other authors.

COMPETING INTERESTS

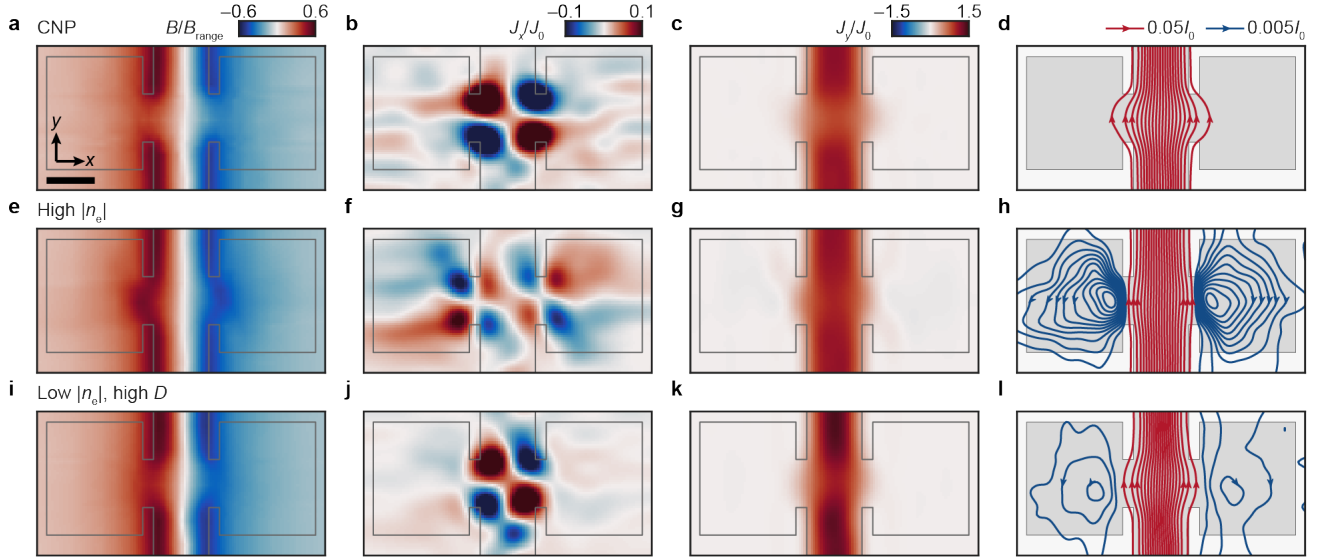
The authors declare no competing interests.

DATA AND CODE AVAILABILITY

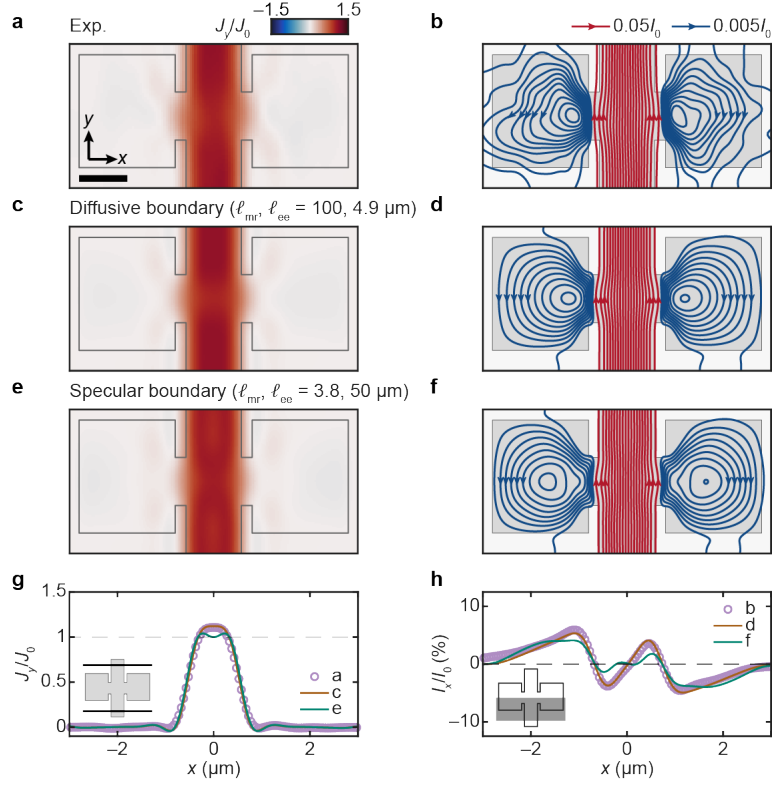
All supporting data and numerical codes for this paper and other findings of this study are available from the corresponding author upon request.



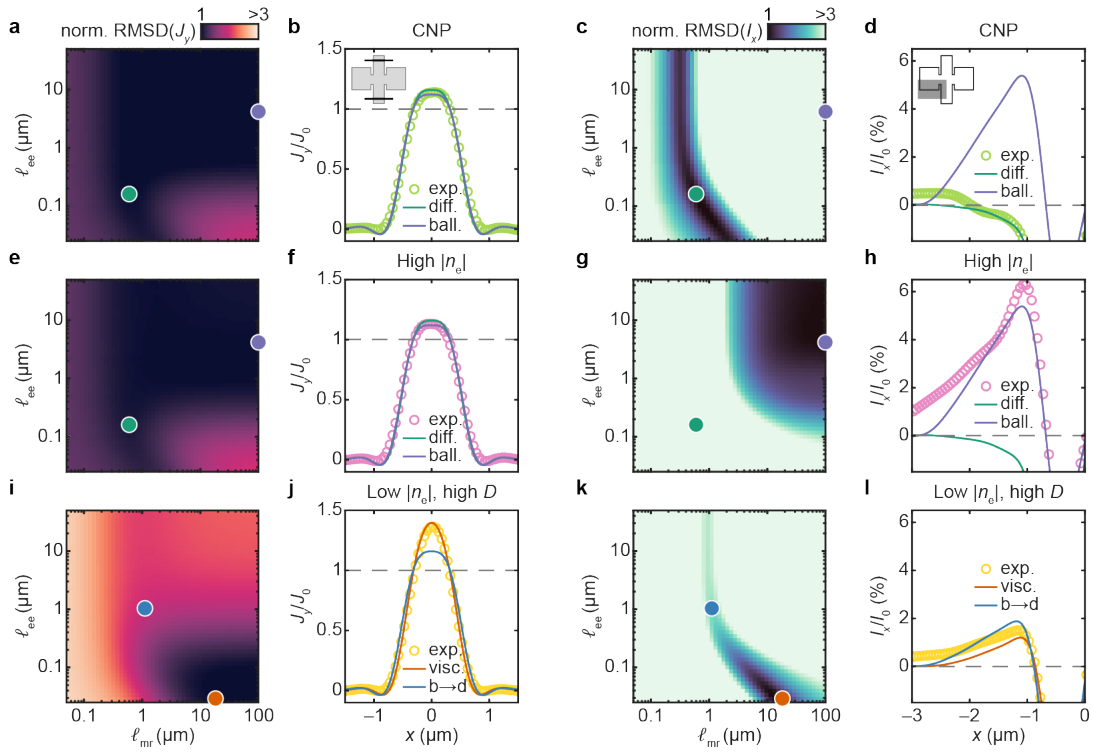
Extended Data Fig. 1. Sample geometry. **a**, Optical image of dual-gated R2G after patterning. Scale bar: $10\ \mu\text{m}$. **b**, Zoomed-in atomic force microscopy (AFM) image of the active region. Scale bar: $1\ \mu\text{m}$.



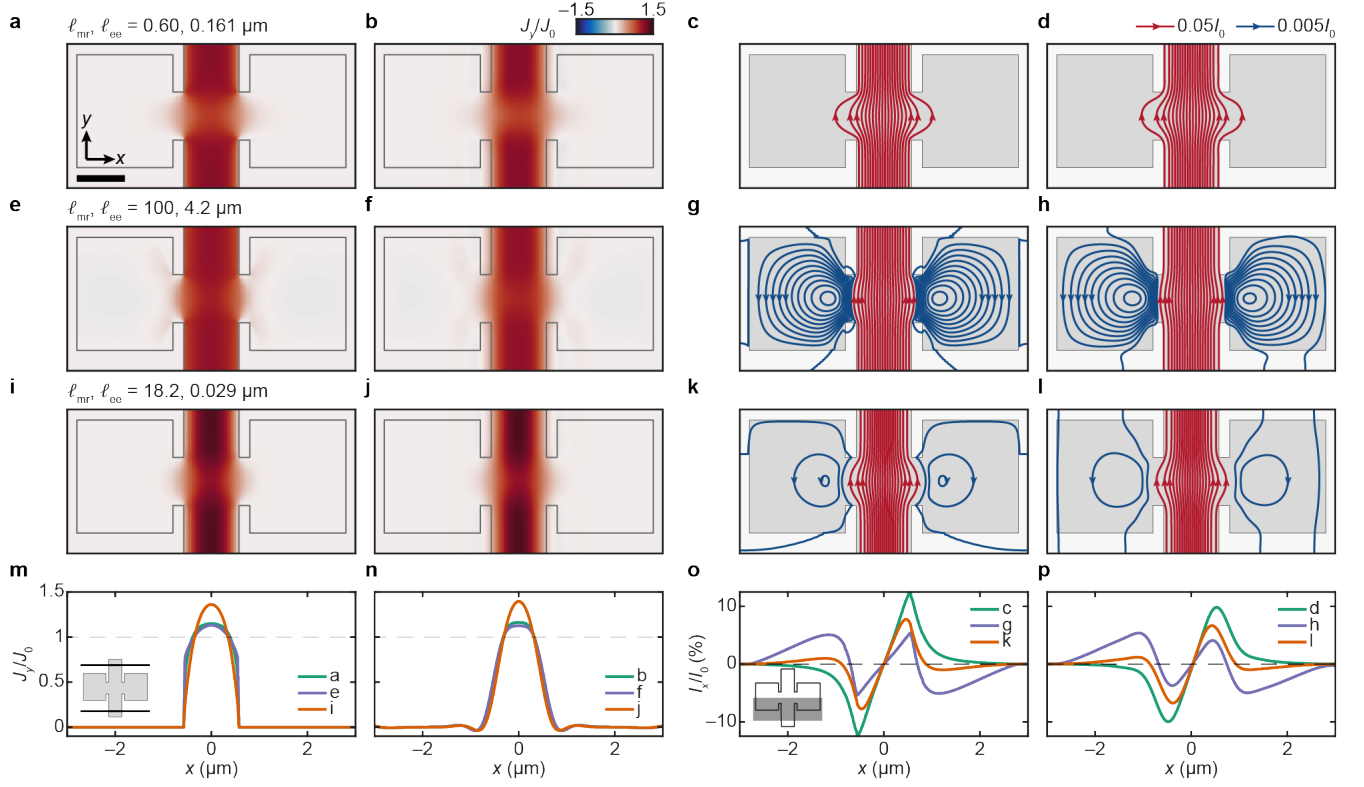
Extended Data Fig. 2. Magnetic field, current density, and current streamline plots for the data in Fig. 2. **a**, Fringe magnetic field signal $B(x, y)$ measured at $n_e = 0 \times 10^{12}\ \text{cm}^{-2}$ and $D = 0\ \text{V/nm}$. Scale bar: $1\ \mu\text{m}$. $B(x, y)$ is normalized by $B_{\text{range}} \equiv B_{\text{max}} - B_{\text{min}}$. **b**, Reconstructed current density $J_x(x, y)$ at the same n_e and D as panel **a**. J_x is normalized by $J_0 \equiv I_0/w$. **c, d**, Reproduction of Fig. 2a, b for comparison. **e**, $B(x, y)$ at $n_e = -1.3 \times 10^{12}\ \text{cm}^{-2}$ and $D = 0.39\ \text{V/nm}$. **f**, $J_x(x, y)$ at the same n_e and D as panel **e**. **g, h**, Reproduction of Fig. 2c, d for comparison. **i**, $B(x, y)$ at $n_e = -0.4 \times 10^{12}\ \text{cm}^{-2}$ and $D = 0.39\ \text{V/nm}$. **j**, $J_x(x, y)$ at the same n_e and D as panel **i**. **k, l**, Reproduction of Fig. 2e, f for comparison.



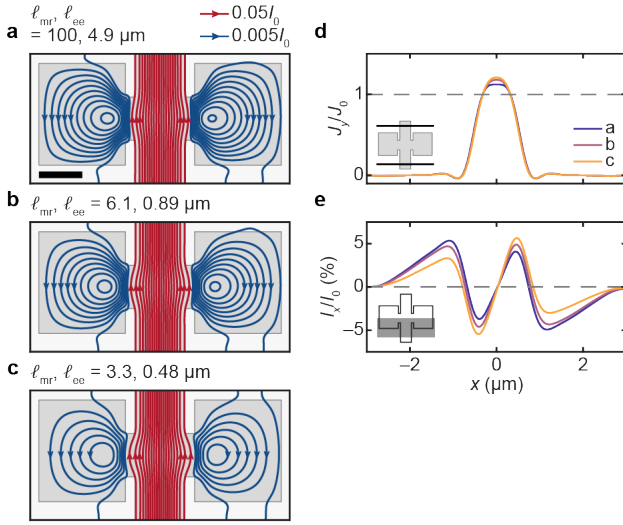
Extended Data Fig. 3. Benchmarking boundary scattering condition. **a**, $J_y(x, y)/J_0$ ($J_0 \equiv I_0/w$) measured at $n_e = -1.5 \times 10^{12} \text{ cm}^{-2}$ and $D = 0.39 \text{ V/nm}$. Scale bar: $1 \mu\text{m}$. **b**, Current streamlines at the same n_e and D as panel **a**. **c**, Theoretical $J_y(x, y)/J_0$ and **d**, streamlines under fully diffusive boundary scattering, for best-fit parameters $\ell_{\text{mr}} = 100 \mu\text{m}$ and $\ell_{\text{ee}} = 4.9 \mu\text{m}$. Similar results are obtained for $\ell_{\text{mr}} \gtrsim 5 \mu\text{m}$ and $\ell_{\text{ee}} \gtrsim 800 \text{ nm}$. **e**, Theoretical $J_y(x, y)/J_0$ and **f**, streamlines under fully specular boundary scattering, for best-fit parameters $\ell_{\text{mr}} = 3.8 \mu\text{m}$ and $\ell_{\text{ee}} = 50 \mu\text{m}$. Similar results are obtained for $\ell_{\text{mr}} \gtrsim 1.5 \mu\text{m}$ and $\ell_{\text{ee}} \gtrsim 300 \text{ nm}$. **g**, $J_y(x, \pm 2 \mu\text{m})/J_0$ corresponding to panels **a**, **c**, and **e**. **h**, $I_x(x)/I_0$ corresponding to panels **b**, **d**, and **f**. Both types of boundary condition constrain ℓ_{mr} and ℓ_{ee} in the deeply ballistic regime, expected under heavy hole doping, but a significant better match to experiment is obtained under diffusive boundary than under specular boundary. Specular boundary is more ill-suited for the low- $|n_e|$ and high- D regime represented by the data of Fig. 2e,f. There, the theoretical flow profile $J_y(x, \pm 2 \mu\text{m})$ becomes insensitive to ℓ_{mr} and ℓ_{ee} , failing to reproduce the observed high current concentration.



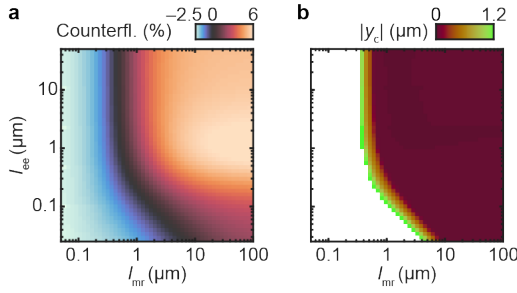
Extended Data Fig. 4. Least squares fitting of $J_y(x)$ and $I_x(x)$. **a**, Root mean square deviation (RMSD) for $J_y(x)/J_0$ between experimental data at $n_e = 0 \times 10^{12} \text{ cm}^{-2}$ and $D = 0 \text{ V/nm}$ and the Boltzmann model parameterized by ℓ_{mr} and ℓ_{ee} . The RMSD is normalized by the minimum value. **b**, Comparison between experimental $J_y(x)/J_0$ and fits in the diffusive and ballistic regimes, using parameters corresponding to dots in panel a. **c**, Normalized RMSD for $I_x(x)/I_0$ at the same n_e and D as panel a. **d**, Comparison between experimental $I_x(x)/I_0$ and fits in the diffusive and ballistic regimes. **e**, Normalized RMSD for $J_y(x)/I_0$ at $n_e = -1.3 \times 10^{12} \text{ cm}^{-2}$ and $D = 0.39 \text{ V/nm}$. **f**, Comparison between experimental $J_y(x)/J_0$ and fits in the diffusive and ballistic regimes. **g**, Normalized RMSD for $I_x(x)/I_0$ at the same n_e and D as panel e. **h**, Comparison between experimental $I_x(x)/I_0$ and fits in the diffusive and ballistic regimes. **i**, Normalized RMSD for $J_y(x)/I_0$ at $n_e = -0.4 \times 10^{12} \text{ cm}^{-2}$ and $D = 0.39 \text{ V/nm}$. **j**, Comparison between experimental $J_y(x)/J_0$ and fits in the viscous (i.e., hydrodynamic) regime as well as at the direct transition between ballistic and diffusive regimes, using parameters corresponding to dots in panel i. **k**, Normalized RMSD for $I_x(x)/I_0$ at the same n_e and D as panel i. **l**, Comparison between experimental $I_x(x)/I_0$ and fits in the viscous regime and at the ballistic-to-diffusive transition.



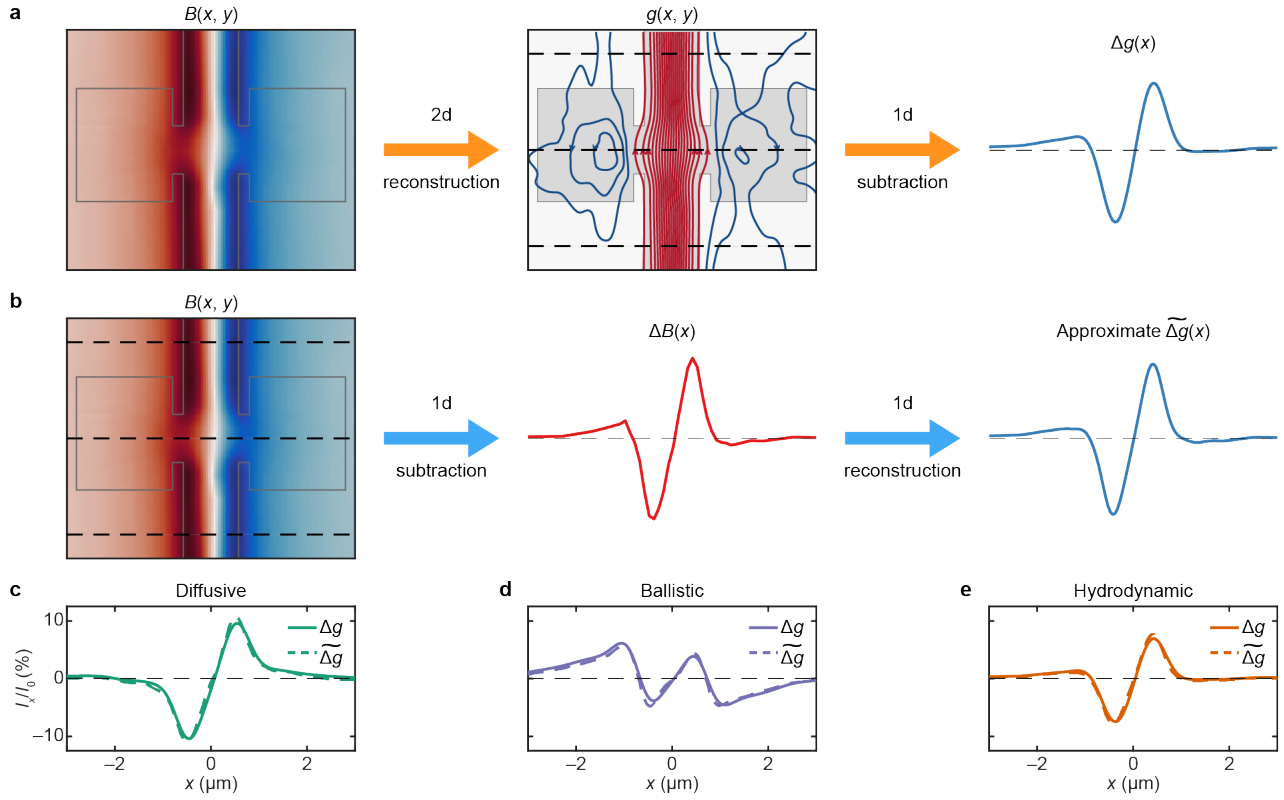
Extended Data Fig. 5. Comparison of directly simulated and reconstructed theoretical current profile. **a**, Directly simulated $J_y(x, y)/J_0$ in the diffusive regime, for $\ell_{\text{mr}} = 600$ nm and $\ell_{\text{ee}} = 161$ nm. Scale bar: $1 \mu\text{m}$. **b**, $J_y(x, y)/J_0$ reconstructed from simulated $B(x, y)$ for the same $(\ell_{\text{mr}}, \ell_{\text{ee}})$ as panel **a**. **c**, Directly simulated current streamlines and **d**, Reconstructed current streamlines for the same $(\ell_{\text{mr}}, \ell_{\text{ee}})$ as panel **a**. **e**, Directly simulated $J_y(x, y)/J_0$ in the ballistic regime, for $\ell_{\text{mr}} = 100 \mu\text{m}$ and $\ell_{\text{ee}} = 4.2 \mu\text{m}$. **f**, Reconstructed $J_y(x, y)/J_0$ for the same $(\ell_{\text{mr}}, \ell_{\text{ee}})$ as panel **e**. **g**, Directly simulated current streamlines and **h**, Reconstructed current streamlines for the same $(\ell_{\text{mr}}, \ell_{\text{ee}})$ as panel **e**. **i**, Directly simulated $J_y(x, y)/J_0$ in the hydrodynamic regime, for $\ell_{\text{mr}} = 18.2 \mu\text{m}$ and $\ell_{\text{ee}} = 29$ nm. **j**, Reconstructed $J_y(x, y)/J_0$ for the same $(\ell_{\text{mr}}, \ell_{\text{ee}})$ as panel **i**. **k**, Directly simulated current streamlines and **l**, Reconstructed current streamlines for the same $(\ell_{\text{mr}}, \ell_{\text{ee}})$ as panel **i**. **m**, $J_y(x, \pm 2 \mu\text{m})/J_0$ corresponding to panels **a**, **e**, and **i**. **n**, $J_y(x, \pm 2 \mu\text{m})/J_0$ corresponding to panels **b**, **f**, and **j**. **o**, $I_x(x)/I_0$ corresponding to panels **c**, **g**, and **k**. **p**, $I_x(x)/I_0$ corresponding to panels **d**, **h**, and **l**.



Extended Data Fig. 6. Simulating current-driven ballistic-to-viscous crossover. **a**, Theoretical current streamlines for $\ell_{\text{mr}} = 100 \mu\text{m}$ and $\ell_{\text{ee}} = 4.9 \mu\text{m}$, corresponding to the best fit for the data of Fig. 4a. Scale bar: $1 \mu\text{m}$. **b**, Theoretical streamlines for $\ell_{\text{mr}} = 6.1 \mu\text{m}$ and $\ell_{\text{ee}} = 890 \text{nm}$, corresponding to the best fit for the data of Fig. 4b. **c**, Theoretical streamlines for $\ell_{\text{mr}} = 3.3 \mu\text{m}$ and $\ell_{\text{ee}} = 480 \text{nm}$, corresponding to the best fit for the data of Fig. 4c. **d**, $J_y(x, \pm 2 \mu\text{m})/J_0$ corresponding to panels a, b, and c. **e**, $I_x(x)/I_0$ corresponding to panels a, b, and c. The increase in channel flow concentration and suppression of vortical flow upon decreasing ℓ_{ee} reproduce the observed current-driven behavior.



Extended Data Fig. 7. Vortex center position within the linearized Boltzmann model. **a**, Counterflow $I_x(|x| = 1.3 \mu\text{m})/I_0$ within the Boltzmann model parameterized by ℓ_{mr} and ℓ_{ee} . **b**, The vortex center position $|y_c|$ (see Methods). No vortices are present in the white region corresponding to negative counterflow in panel a.



Extended Data Fig. 8. Comparison of full 2d current reconstruction and simplified 1d reconstruction. **a**, 2d $g(x, y)$ map is inverted from $B(x, y)$ using the full kernel (4), and $\Delta g(x)$ is obtained by subtracting it along three 1d trajectories (Eq. 10). **b**, Approximate $\tilde{\Delta g}(x)$ is directly inverted from $\Delta B(x)$ using the effective 1d kernel (12) ($l_y = 3 \mu\text{m}$). **c**, Comparison between normalized $\Delta g(x)$ and $\tilde{\Delta g}(x)$ (i.e., $I(x)/I_0$) at $n_e = 0 \times 10^{12} \text{ cm}^{-2}$ and $D = 0 \text{ V/nm}$ (diffusive regime). **d**, Comparison between $\Delta g(x)$ and $\tilde{\Delta g}(x)$ at $n_e = -1.3 \times 10^{12} \text{ cm}^{-2}$ and $D = 0.39 \text{ V/nm}$ (ballistic regime). **e**, Comparison between $\Delta g(x)$ and $\tilde{\Delta g}(x)$ at $n_e = -0.4 \times 10^{12} \text{ cm}^{-2}$ and $D = 0.39 \text{ V/nm}$ (hydrodynamic regime).

Extended Data Video 1. Current-driven vortex deformation. Evolution of current streamlines at $n_e = -0.25 \times 10^{12} \text{ cm}^{-2}$ and $D = 0 \text{ V/nm}$ upon increasing I_0 from 27 to 100 μA . Scale bar: 1 μm . 1 red line = $0.05I_0$, 1 solid blue line = $0.005I_0$. Additional dashed streamlines serve as guides to the eye.